Double Etch Method for the Fabrication of Nanophotonic Devices from Van der Waals Materials

Otto Cranwell Schaeper[1,2], Lesley Spencer[1,2], Dominic Scognamiglio[1], Waleed El-Sayed[3], Benjamin Whitefield[1,2], Jake Horder[1,2], Nathan Coste[1], Paul Barclay[3,4,5], Milos Toth[1,2], Anastasiia Zalogina[1,2*], and Igor Aharonovich[1,2*]

[1] *School of Mathematical and Physical Sciences, University of Technology Sydney, Ultimo, New South Wales 2007, Australia*

[2] *ARC Centre of Excellence for Transformative Meta-Optical Systems, University of Technology Sydney, Ultimo, New South Wales 2007, Australia*

[3] *Institute for Quantum Science and Technology, University of Calgary, Calgary, AB T2N 1N4, Canada*

[4] *Department of Physics and Astronomy, University of Calgary, Calgary, AB T2N 1N4, Canada*

[5] *Nanotechnology Research Centre, National Research Council of Canada, Edmonton, AB T6Gf 2M9, Canada*

[*]anastasiia.zalogina@uts.edu.au; igor.aharonovich@uts.edu.au

Abstract

The integration of van der Waals (vdW) materials into photonic devices has laid out a foundation for many new quantum and optoelectronic applications. Despite tremendous progress in the nanofabrication of photonic building blocks from vdW crystals, there are still limitations, specifically with large-area devices and masking. Here, we focus on hexagonal boron nitride (hBN) as a vdW material and present a double etch method that overcomes problems associated with methods that employ metallic films and resist-based films for masking. Efficacy of the developed protocol is demonstrated by designing and fabricating a set of functional photonic components – including waveguides, ring resonators and photonic crystal cavities. The functionality of the fabricated structures is demonstrated through optical characterization over several key spectral ranges. These include the near-infrared and blue ranges, where the hBN boron vacancy (V_B^-) spin defects and the coherent B center quantum emitters emit, respectively. The double etch method enables fabrication of high-quality factor optical cavities and constitutes a promising pathway toward on-chip integration of vdW materials.

KEYWORDS: hexagonal boron nitride, van der Waals materials, fabrication.

Integrated quantum photonics has attracted significant attention by introducing photons as qubits that are robust against decoherence, and by using resonant structures for photon manipulation [1-6]. Confinement and control of light at the nanoscale require advanced protocols for the nanofabrication of photonic building blocks, including waveguides, cavities and resonators . In recent years, van der Waals (vdW) crystals have emerged as a promising platform for quantum photonic devices [7-14]. For example, transition metal dichalcogenides offer a combination of nonlinear effects and a high refractive index, which is advantageous for light confinement and photon guiding [14].

Hexagonal boron nitride (hBN) is particularly attractive as a vdW material for quantum applications[15]. Due to its wide bandgap of ~6 eV, it can host a variety of ultra-bright optically active defects that operate at room temperature and are suitable for quantum information processing [16-21]. In addition, hBN also hosts ensembles of spin defects that are of interest for quantum sensing [22-26]. Some of these defects can be engineered deterministically with reproducible emission wavelengths which is crucial for scalability of on-chip devices [16]. A key challenge in utilizing these defects in practical on-chip devices is coupling them to the modes of nanostructures used to generate, manipulate and collect the emitted photons. These nanostructures include waveguides, ring resonators, nanobeam photonic crystal cavities, metasurfaces or topological photonic structures[2, 4]. By using structures made from vdW materials like hBN, we can ensure that the emitters are located within the nanostructures, where the highest electromagnetic field confinement occurs [27-29]. This positioning maximizes coupling efficiency, even if the defect is slightly off the point of maximum field confinement[29]. However, the challenge of monolithic fabrication using the same material as the emitter's host remains, which is why some approaches involve placing flakes of vdW materials with emitters on top of the structures [29-31]. Despite these challenges, once the emitter is within the cavity of the photonic structure, it remains stable, making this approach promising for large-scale integration.

In the current work, we present a fabrication method tailored for vdW materials, employing a double etch approach for mask transfer using an ion beam etcher (IBE) and an inductively coupled plasma reactive ion etcher (ICP RIE). This method addresses limitations of existing vdW material nanofabrication protocols that employ metallic films and resist films for masking (more information about these limitations is provided in the Supplementary Information, see Figures S1-S4). The novelty of the double etch method lies in its ability to fabricate devices from thicker vdW materials, its potential for large-scale fabrication, ease of suspended structures engineering and potentially easier mask removal – all of which addresses significant scalability issues.

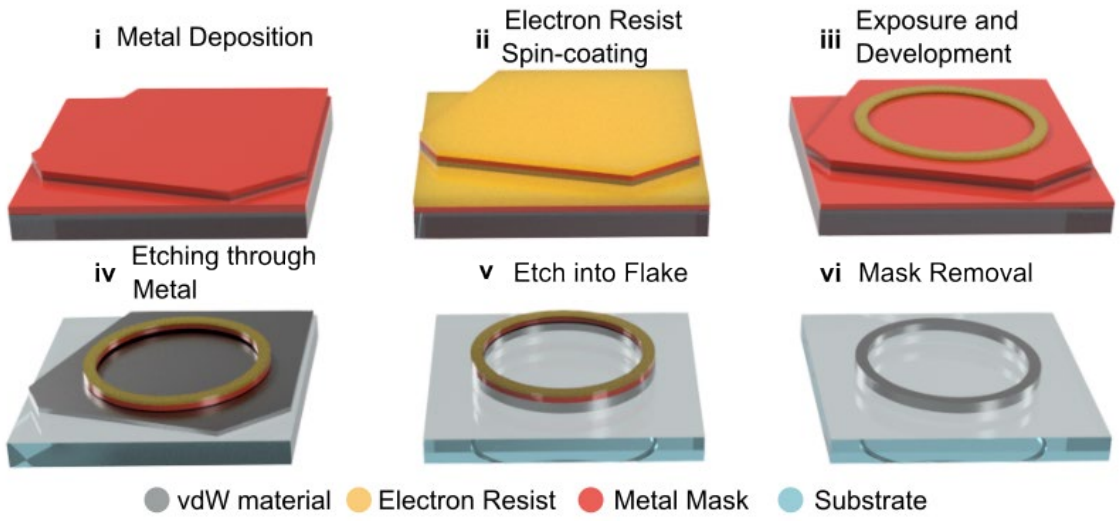

Figure 1. Schematic of the double etch protocol. *(i) Metal deposition onto an exfoliated flake of hBN. (ii) Electron-beam resist spin-coating. (iii) Resist exposure and development. (iv) First*

etching step through the exposed metal mask using IBE. (v) Second etching step through vdW material using ICP RIE. (vi) Metal mask and resist removal.

The developed double etch method is based on the complementary etching chemistries used to transfer patterns from an electron-beam resist into tungsten via a fluorine etch. This method eliminates the need for sonication and lift-off, making it compatible with vdW materials. This is crucial, because unlike nanofabrication of 3D materials, vdW crystals can easily get lost during the sonication process by disconnecting from the substrate. The double etch fabrication protocol is illustrated schematically in Figure 1. First, a vdW flake is coated homogeneously with a layer of metal (i), followed by spin-coating of an electron-beam resist (ii). Here, a positive tone resist polymethyl methacrylate (PMMA) of 300 nm is used due to its good balance of sensitivity and contrast[32], while maintaining the electron beam lithography patterning time nearly the same as for positive tone resist by inverting the design and limiting the exposure by creating a box around the pattern (see Figure 2). A pattern is then defined in the resist, where the unexposed resist becomes the region protected by the metal (iii). The resist layer now acts as a hard mask for etching the metal using ICP RIE (iv), eliminating the risk associated with the lift-off process, which often leads to removal and loss of the flake. Given the physical nature of IBE, the resist layer must be sufficiently thick and resistant to IBE etching. Next, the vdW material is etched using ICP RIE through the created double mask of resist and metal (v). Finally, the double mask is removed using a mixture of sulfuric acid and hydrogen peroxide (piranha solution) (vi). See the methods section and the SI for more details. Note that conventionally, a hard mask is used with an intermediate adhesive layer between the resist and metal layers. Here, the metal hard mask coats the entire sample uniformly, eliminating the need for an adhesive layer and simplifying both the metal deposition and removal steps.

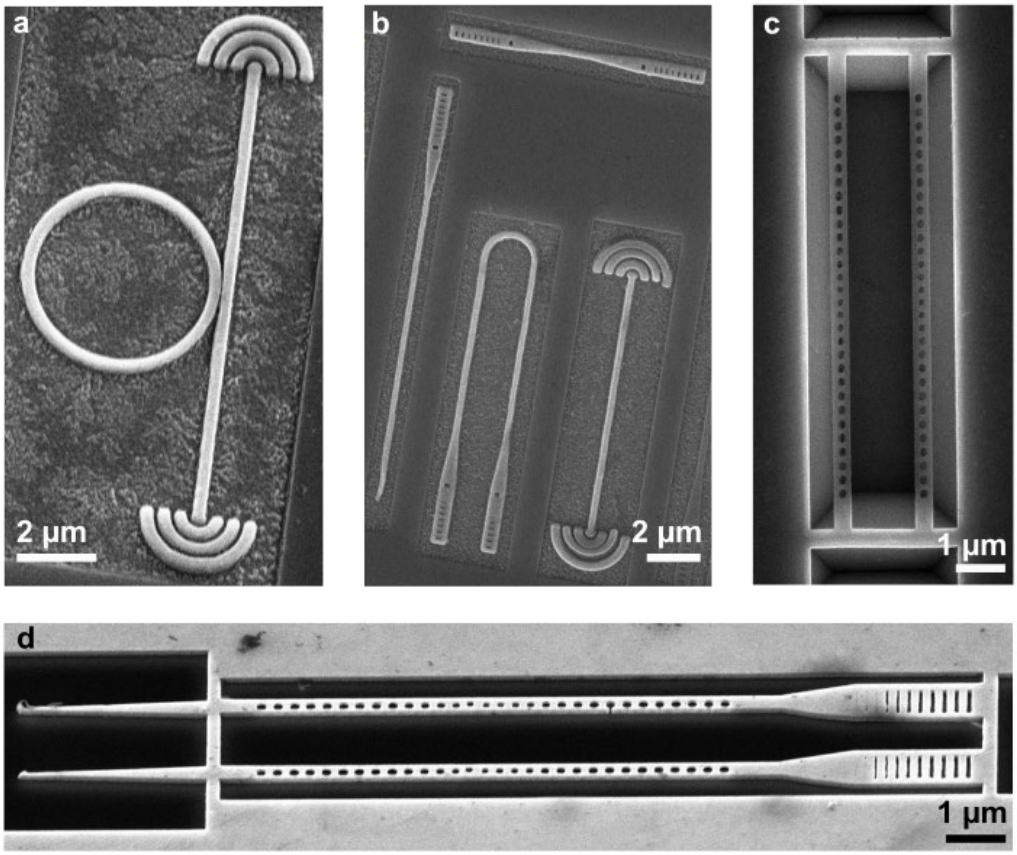

Figure 2. Scanning electron microscope images of photonic devices fabricated from hBN using the double etch method. *(a) Microring resonator coupled to a bus waveguide. (b) Four different waveguide geometries, including one with a bend geometry. (c) Undercut one-dimensional (1D) photonic crystal cavities (PCC) (d) 1D PCC waveguides with tapered ends and grating couplers.*

To demonstrate the utility of the double etch method, we designed and fabricated photonic components with various architectures hosting emitters at different emission wavelengths. For clarity and usefulness, we focus on two regions of interest in hBN: (1) the near-infrared region, where the spin-active boron vacancy (V_B^-) defects emit and (2) the blue spectral range where the B centers with a zero phonon line (ZPL) at 436 nm emit. The B centers are currently the most promising for deployment in quantum information protocols due to their coherent properties, hence we fabricated devices in this spectral range [17, 33, 34]. Lastly, we also fabricate a one-dimensional (1D) photonic crystal cavity (PCC) with a resonance in the infrared range, which has not been realized previously using hBN. These functional nanostructures are foundational to future hBN quantum circuitry and offer opportunities for scalable, reproducible, and robust on-chip devices, overcoming challenges with existing vdW material fabrication methods.

Figure 2 shows scanning electron microscope (SEM) images of these devices. All structures are based on hBN material exfoliated onto a Si substrate with a dissipative SiO_2 layer. Different thicknesses of hBN flakes were chosen to maximize light confinement within the designed photonic structures. The microring resonator in Figure 2 (a) is designed to host V_B^- defects emitting at 760 nm (1.6 eV) (see additional SEM images of this device in Figure S6 of the

Supplementary Information). Given that V_B^- defects exhibit broad emission, ring resonators are particularly well-suited for these emitters. They can support multimode whispering gallery modes with a small free spectral range, eliminating the need for scaling parameters to match a ZPL[35]. The microring resonator, with a diameter of 5 μm, is coupled to a 12-μm long bus waveguide with couplers through a 75-nm gap, measured using an SEM image. This small gap enables efficient coupling from the resonator to the waveguide. Both the bus waveguide and the ring resonator were fabricated with a width of 200-nm. Such structures are designed for on-chip distributed quantum sensing applications discussed further in Figure 3.

A set of different waveguides for guiding single photons, featuring variously shaped Bragg grating couplers for efficient excitation and collection, are shown in Figure 2 (b). These waveguides are designed to contain B centers with an emission wavelength of 436 nm (2.8 eV) created using electron beam irradiation[16]. In contrast to V_B^- defects, B centers possess a ZPL, allowing the waveguides to be engineered with a mode that efficiently couples to this emission wavelength. Each waveguide has dimensions of 200 nm in width and thickness, ensuring good confinement for light guiding at the wavelength of 436 nm.

To showcase the versatility of the double etch method, we fabricated a larger 1D PCC structure at longer wavelengths to explore the telecom range. Figure 2 (c) shows an example of a 1D PCC (see additional SEM images of this device in Figure S7 (a) and (b) of the Supplementary Information). This particular cavity was undercut using a potassium hydroxide solution (KOH), creating an air gap and eliminating the need for the SiO_2 layer. An SEM image where the sample has been tilted to 45° is provided in the Supplementary Information as Figure S9. Here, the use of a positive resist comes as an advantage. Using a positive resist allows for a minimal area to be patterned, whilst allowing the structure to be connected to the largest region possible - the entire flake. The reason for connecting the structure to the entire flake is to enhance the undercutting process. These undercut cavities were fabricated to function as optomechanical systems and are suitable for studying thermally driven mechanical resonance in the near-infrared range[36]. To explore this range, we designed a 1D PCC structure with an optical band gap around 1600 nm, achieving high sensitivity by co-localizing optical and mechanical modes. The careful design of gap and hole parameters allowed us to localize the optical field in the central region, enhancing optomechanical coupling, which is valuable for optomechanical applications (The design parameters are shown in the Supplementary Information Figure S10). Finally, one of the most critical nanophotonic structures - a tapered waveguide with a 1D PCC and a Bragg grating coupler, is demonstrated in Figure 2 (d) [2, 37-39] (see an additional SEM image of this device in Figure S7 (c) of the Supplementary Information). These structures are often employed for highly efficient side collection with a matching tapered single mode fiber.

To characterize the functionalities of the fabricated photonic devices, we measured a microring resonator containing the V_B^- spin defects. Two different excitation configurations were used when measuring this structure, as shown in the schematics in Figure 3 (a, b). In the first configuration we excited the devices through one of the couplers and collected through the other coupler. In the second configuration we directly excited the V_B^- spin defects on the ring and collected through the coupler. In both excitation methods, multiple V_B^- defects are excited,

as a single emitter would be too weak to detect reliably. Photoluminescence (PL) measurements were performed using a lab-built scanning PL setup featuring decoupled excitation and collection. The device was excited using a 532 continuous wave (CW) laser through a 100X 0.9 NA objective and was collected through the same objective.

The spectra in Figure 3 (c, d) conclusively show that the devices operate as intended. The V_B^- defects exhibit the broad emission centered at around 760 nm. Whispering gallery modes (WGMs) are clearly visible and evident as sharp peaks within the spectrum. The higher periodicity of WGMs at shorter wavelengths in Figure 3 (c) is due to the presence of the second order modes. The quality factor of the WGMs is defined here as $Q = \lambda/\Delta\lambda$ (where λ is a resonant wavelength, and $\Delta\lambda$ is a full width at half maximum). The measured Q is ~300 at 683 nm for the current set of devices, the peak is indicated by the red arrow in Figure 3 (b). The Q of the resonators can be further improved by undercutting the structures or fabricating larger resonators. However, surface roughness and fabrication imperfections may introduce additional losses reducing the final Q.

In Figure 3 (c) and (d), there is a reduction in the spectra intensity around ~ 730 nm, since the excitation in (c) is done through the waveguide. The emission in these hBN devices originates from broad V_B^- emission around 780 nm and a broad background emission inherent to the hBN material that is centered at ~ 650 nm. Consequently, there is less luminescence at ~ 730 nm. This is a property of the hBN, rather than the microrings.

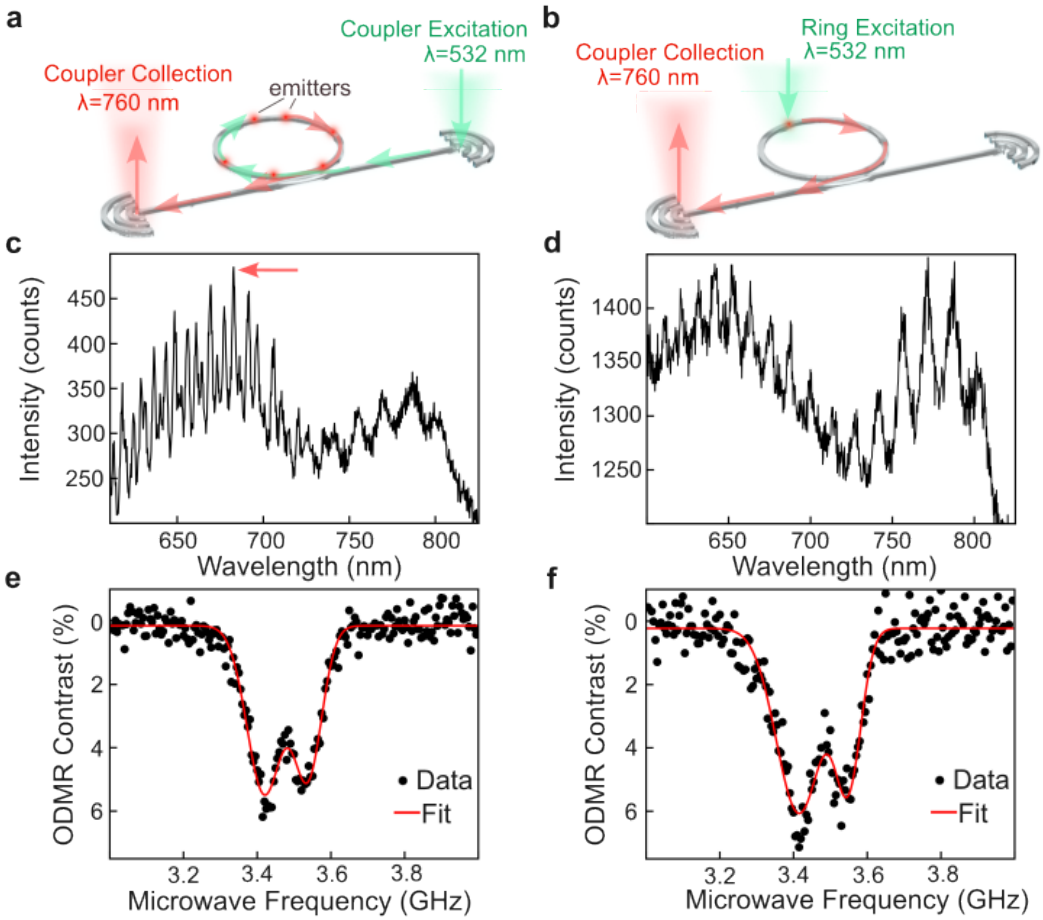

Figure 3. On-chip distributed quantum sensing. *Schematics of two excitation schemes of the V_B^- defects: excitation through the bus waveguide (a), and direct excitation from the microring (b). Collection in both cases is done using the second coupler. (c, d) Photoluminescence (PL) intensity spectra, collected using both configurations (excitation through the bus waveguide and excitation from the ring). The broad emission around ~760 nm corresponds to the V_B^- ensemble, and the sharp peaks are the WGMs. The red arrow in (c) indicates the peak used for the calculation of the quality factor. (e, f) Optically detected magnetic resonance (ODMR) of the V_B^- spin defects measured at zero magnetic field under the same configurations.*

With this device, we further demonstrate on-chip distributed quantum sensing measurement via optically detected magnetic resonance (ODMR) of the V_B^- defects embedded in the microring. Using the same setup configurations as mentioned above (Figure 3 (a, b)), we collected the ODMR signal by measuring the emission intensity difference as the microwave signal is swept across the V_B^- ground state (see Methods). The double dip at ~3.4 and 3.55 GHz corresponds to the splitting of the ground state of the V_B^- ensemble and serves as a signature for magnetic field sensing [20]. An ODMR contrast of ~6% was obtained for both configurations (Figure 3 (e, f)), which shows that there is no degradation in OMDR contrast within the device. Importantly, the V_B^- defects are excited equally well both from the top of the microring, as well as through the bus waveguide. The latter offers a unique feature whereby the devices can probe magnetic fields in a delocalized geometry, where the excitation and collection is performed through couplers and bus waveguides [40]. Such an approach enables distributed quantum sensing across a larger area of the chip employing several large coupled microring resonators, which will become feasible.

We now turn to the waveguides designed to host emitters in the blue spectral range (B centers), with a ZPL at ~436 nm. After fabrication, B centers were deterministically placed by electron beam irradiation and resonant excitation (photoluminescence excitation (PLE)) was performed. Observing a narrow linewidth from resonant excitation is important for future Hong-Ou-Mandel experiments as well as advanced quantum optics measurements[17, 41]. The device is shown in Figure 4 (a): the emitter is resonantly excited (light blue) and its emission is collected (dark blue) through the same coupler. A mirror at the opposite end of the waveguide allows for increased collection efficiency. This measurement is carried out at 5 K. We measure the emission from the phonon sideband as a function of the laser detuning to the center of the ZPL. The results are displayed as the black circles in Figure 4 (b). The same experiment was repeated by exciting and collecting directly on top of the emitter (blue circles in Figure 4 (b)). The excitation and collection of the B center through the coupler yielded a resonant linewidth of ~7.7 GHz, whereas excitation and collection on top of the emitter resulted in a slightly broader line of ~8.5 GHz. The slightly broader linewidth observed when excitation and collection occur on top of the emitter is likely due to variations in excitation power, as precise matching between two excitation configurations can be challenging. The inset of Figure 4 (b) shows a spectrum of waveguide emission from the coupler under off-resonant (405 nm) excitation, showing the ZPL of the emitter (at room temperature).

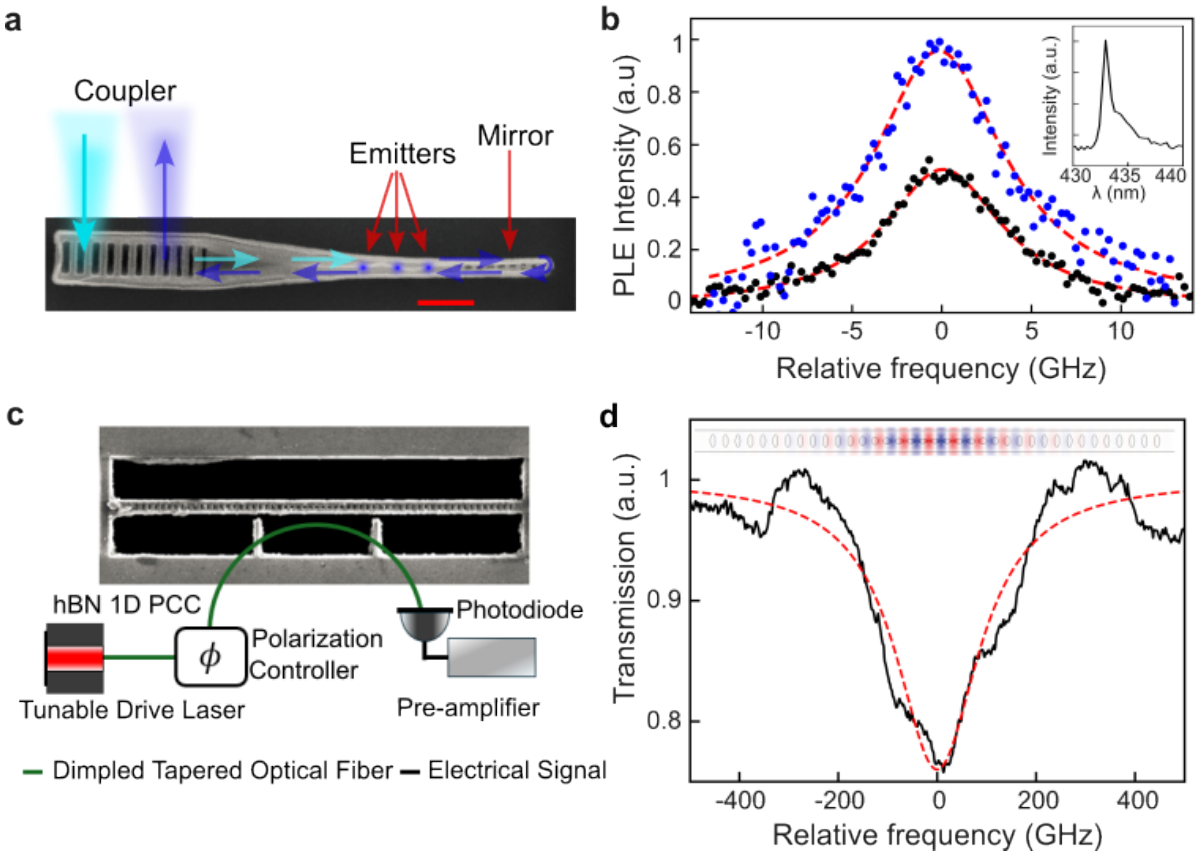

Figure 4. Optical characterization of fabricated devices*. (a) SEM image with the schematic of excitation (light blue) and the collection (blue) of B centers. Scale bar is 1 µm. (b) Resonant photoluminescence excitation (PLE) spectra for the emitters excited through the waveguide (filled black circles) and excited and collected from the same spot (filled blue circles) collected at 5K. Inset: Photoluminescence (PL) spectrum collected at room temperature. (c) Schematic of the optical setup used to measure the 1D PCC with SEM of 1D PCC image at the top. Scale bar is 5 µm. (d) Transmission spectrum. The estimated Q factor from this spectrum is ~1000. The inset: numerical simulation of the optical mode localized in the device.*

Finally, we test the 1D PCC at the telecom range. The main motivation to fabricate hBN resonators at the telecom range is to explore optomechanical effects of hBN cavities. This is typically done with tunable narrowband IR laser, and requires sharp optical and mechanical resonances[42, 43]. This range remains unexplored since there have not been found emitters in hBN. We demonstrate the first evidence of a high Q cavity at ~1600 nm. A careful design of the geometrical parameters of the gaps and holes in the 1D PCC allows the optical mode to be localized in the central region (see the inset at the top of Figure 4 (d)). Figure 4 (c) shows the schematic of the setup used to measure this device. Laser light is sent into a dimpled tapered optical fiber, which evanescently couples into the beam cavity when positioned in a close proximity. The laser frequency is then scanned from 1500 to 1700 nm. The transmission spectrum is measured using a photodetector. For the fabricated device (SEM image at the top of Figure 4 (c)), we obtained an intrinsic Q of ~1000 at the wavelength of ~1600 nm, as shown in Figure 4 (d).

To conclude, we introduced a double-etching method to fabricate scalable photonic devices from vdW materials and demonstrated it with hBN. We fabricated cavities and microring resonators with bus waveguides, that are suitable to be deployed for quantum circuitry. A key advantage of this method is elimination of the need of lift-off or sonication during the fabrication process. Using the double etching method, we realized both on-chip distributed quantum sensing with V_B^- defects as well as coherent excitation of the B centers. Furthermore, we showed that the method is suitable to engineer high-Q cavities for the telecom range that had not been realized to date. Such fundamental advances in fabrication could be applicable to other vdW materials, particularly TMDCs, thereby opening up possibilities for compact and efficient quantum photonic devices.

Methods

Fabrication. Pristine hBN flakes sourced from the National Institute for Materials Science (NIMS) were mechanically exfoliated using scotch tape and then transferred using Gel-Pak strips onto 285-nm SiO_2 on Si substrates. These samples were annealed in a tube furnace (Lindberg/Blue 500 Mini-Mite) in an ambient atmosphere at temperatures of 500°C, 650°C, and 850°C to create B centers in hBN as well as increase the adhesion of the hBN flakes to the sample surface and remove the polymer contamination. Exfoliated hBN flakes for the set of waveguides in Figure 2 (b) were annealed on a hot plate instead, at 500°C, to remove the polymer contamination. Next, hBN flakes were preselected based on the thickness requirements for fabrication using an optical microscope. A 25-nm layer of nickel is then deposited across the substrate and hBN flakes using an electron beam evaporator (AJA ATC-1800E). A layer of electron-beam resist polymethyl methacrylate (PMMA) A5 (AllResist gmbh) was spin-coated on the sample at 5000 rpm for 30 s resulting in a layer of polymer ~300 nm thick, the sample was then baked at 180°C for three minutes. The polymer was then patterned using electron beam lithography (Elionix ELS-F125) at 125 kV and 1 nA. Next, the exposed pattern was developed in 1:3 IPA:MIBK for 60 s, rinsed in IPA for 20 s, and gently dried with a nitrogen gun (see details on flakes submerging in solutions and drying in Figure S5, Section S4 of the Supplementary Information). Following the development, the pattern is transferred by the use of an ion beam etcher (Intlvac) at 6 sccm Ar, 1.5 A of discharge, 0.150 A of emission to the LFN, 12 sccm of Ar to the ion source, 400 V beam voltage, 150 mA beam current, 60 V accelerator voltage, with a stage temperature of 20°C for 90 s. The nickel and any remaining resist then act as the hard mask when the mask is transferred into the hBN using a reactive ion etching in ICP-RIE system (Trion) at 1 mT, 5 sccm SF_6, 60 sccm Ar, 300W RF and 1W ICP with the etch rate of ~5 nm/s. Then the nickel mask is removed using piranha solution (3:1 sulphuric acid: hydrogen peroxide) at room temperature. In order to make it more compatible with other vdW materials, the nickel mask can be removed using either dilute nitric acid (~20%) or chromium etchant. Once the nickel mask had been removed, a dual beam system was used to implant both V_B^- and B center emitters (Thermo Fisher Scientific Helios G4). V_B^- centers were implanted in the microring (Figure 2 (a)), using a 30 keV nitrogen ion beam to irradiate an area with a fluence of 1×10^{14} ions/cm^2. B centers were implanted using

a 3 keV, 1.6 nA electron beam with a 5 ms dwell time. The dwell time was varied over multiple waveguides to achieve an electron dose of 7.5×10^{10} to 2×10^{11}.

This fabrication method was also used to fabricate a structure from WS_2 following the exact same process as above, but critically using chromium etchant to remove the nickel layer. The fabricated device is shown in Figure S8 of the Supplementary Information.

Photoluminescence Measurements. V_B^- emission was measured using a lab-built confocal microscopy setup with a fixed 532 CW laser excitation. A 4F system and scanning mirror allowed for decoupling of the collection from the excitation. A 100X 0.9 NA objective (Nikon) was used for both excitation and collection, directing light to a spectrometer (Princeton Instruments Acton SP2300) or an avalanche photodiode (APD) (Excelitas SPCM AQRH-14-FC) through a multimode fiber. B center emission was measured using a lab-built confocal microscopy setup with 0.82 NA objective lens (Attocube). Resonant excitation was performed with a frequency doubled Ti:sapphire scanning laser (M Squared) scanned at a rate of 1 GHz/s. Photons from the phonon sideband were collected with a 442 nm long-pass filter and directed to a spectrometer (Andor) or an APD through a multimode fiber.

Optically Detected Magnetic Resonance (ODMR). Continuous wave ODMR was performed on the V_B^- ensemble by sweeping a radio frequency (RF) signal from 3 to 4 GHz. The RF signal was supplied by a copper wire antenna suspended above the sample. At frequencies of 3.4 and 3.55 GHz, the electron spin is driven between the $m_s = 0$ to -1 and the $m_s = 0$ to $+1$ respectively. The electron is then excited through 532 nm optical pumping resulting in a spin dependent decay and leading to a decrease in photon counts when the spin transitions are driven. The frequency sweep alternated between RF on and off for signal and reference measurements. The photon counts for each frequency were collected by an avalanche photodiode (APD) and the ODMR contrast percentage was then calculated using the equation: Contrast (%) = (Signal-Reference)/Reference × 100. All ODMR measurements were completed at zero external magnetic field and fitted with a double Gaussian curve.

Supporting Information

This work is published with a supporting information file that contains an expanded explanation of the double etch method, along with a deeper comparison of the metal and resist masking methods and a more detailed analysis of their limitations.

Acknowledgments

We thank Angus Gale and Karin Yamamura for assistance with the ion/electron irradiation for emitter creation. We thank Milad Nonahal and Giorge Gemisis for all the advice they provided. The authors acknowledge Takashi Taniguchi (the National Institute for Materials Science) for providing hBN crystal. The authors acknowledge the use of the fabrication facilities as well as scientific and technical assistance from the Research and Prototype Foundry Core Research Facility at the University of Sydney, being a part of the NCRIS-enabled Australian National Fabrication Facility (ANFF), and the UTS facilities, being a part of the ANFF-NSW node.

Funding Sources
The authors acknowledge financial support from the Australian Research Council (CE200100010, FT220100053) and the Office of Naval Research Global (N62909-22-1-2028).

Associated Content
Otto Cranwell Schaeper, Lesley Spencer, Dominic Scognamiglio, Waleed El-Sayed, Benjamin Whitefield, Jake Horder, Nathan Coste, Paul Barclay, Milos Toth, Anastasiia Zalogina, and Igor Aharonovich, *Double Etch Method for the Fabrication of Nanophotonic Devices from Van der Waals Materials* arxiv https://arxiv.org/abs/2407.13475 (accessed november 6th 2024)

References

1. Atatüre, M., et al., *Material platforms for spin-based photonic quantum technologies.* Nature reviews. Materials, 2018. **3**(5): p. 38-51.
2. Kim, J.-H., et al., *Hybrid integration methods for on-chip quantum photonics.* Optica, 2020. **7**(4): p. 291.
3. Lukin, D.M., et al., *4H-silicon-carbide-on-insulator for integrated quantum and nonlinear photonics.* Nature photonics, 2020. **14**(5): p. 330-334.
4. Pelucchi, E., et al., *The potential and global outlook of integrated photonics for quantum technologies.* Nature reviews physics, 2022. **4**(3): p. 194-208.
5. Wan, N.H., et al., *Large-scale integration of artificial atoms in hybrid photonic circuits.* Nature (London), 2020. **583**(7815): p. 226-231.
6. Wang, J., et al., *Integrated photonic quantum technologies.* Nature Photonics, 2020. **14**(5): p. 273-284.
7. Iff, O., et al., *Purcell-Enhanced Single Photon Source Based on a Deterministically Placed WSe2 Monolayer Quantum Dot in a Circular Bragg Grating Cavity.* Nano letters, 2021. **21**(11): p. 4715-4720.
8. Meng, Y., et al., *Photonic van der Waals integration from 2D materials to 3D nanomembranes.* Nature Reviews Materials, 2023. **8**(8): p. 498-517.
9. Parto, K., et al., *Cavity-Enhanced 2D Material Quantum Emitters Deterministically Integrated with Silicon Nitride Microresonators.* Nano Letters, 2022. **22**(23): p. 9748-9756.
10. Schneider, C., et al., *Two-dimensional semiconductors in the regime of strong light-matter coupling.* Nature Communications, 2018. **9**(1).
11. Verre, R., et al., *Transition metal dichalcogenide nanodisks as high-index dielectric Mie nanoresonators.* Nature Nanotechnology, 2019. **14**(7): p. 679-683.
12. Ling, H., et al., *Deeply subwavelength integrated excitonic van der Waals nanophotonics.* Optica, 2023. **10**(10): p. 1345-1352.
13. Liu, C.-H., et al., *Ultrathin van der Waals Metalenses.* Nano letters, 2018. **18**(11): p. 6961-6966.
14. Zotev, P.G., et al., *Van der Waals Materials for Applications in Nanophotonics.* Laser & Photonics Reviews, 2023. **17**(8).
15. Caldwell, J.D., et al., *Photonics with hexagonal boron nitride.* Nature Reviews Materials, 2019. **4**(8): p. 552-567.
16. Aharonovich, I., J.-P. Tetienne, and M. Toth, *Quantum Emitters in Hexagonal Boron Nitride.* Nano letters, 2022. **22**(23): p. 9227-9235.

17. Fournier, C., et al., *Two-Photon Interference from a Quantum Emitter in Hexagonal Boron Nitride.* Physical Review Applied, 2023. **19**(4).
18. Guo, N.-J., et al., *Coherent control of an ultrabright single spin in hexagonal boron nitride at room temperature.* Nature Communications, 2023. **14**(1).
19. Stern, H.L., et al., *A quantum coherent spin in hexagonal boron nitride at ambient conditions.* Nature Materials, 2024.
20. Vogl, T., et al., *Compact Cavity-Enhanced Single-Photon Generation with Hexagonal Boron Nitride.* ACS photonics, 2019. **6**(8): p. 1955-1962.
21. Xu, X., et al., *Creating Quantum Emitters in Hexagonal Boron Nitride Deterministically on Chip-Compatible Substrates.* Nano letters, 2021. **21**(19): p. 8182-8189.
22. Gao, X., et al., *Quantum Sensing of Paramagnetic Spins in Liquids with Spin Qubits in Hexagonal Boron Nitride.* ACS photonics, 2023. **10**(8): p. 2894-2900.
23. Gottscholl, A., et al., *Initialization and read-out of intrinsic spin defects in a van der Waals crystal at room temperature.* Nature Materials, 2020. **19**(5): p. 540-545.
24. Healey, A.J., et al., *Quantum microscopy with van der Waals heterostructures.* Nature physics, 2023. **19**(1): p. 87-91.
25. Vaidya, S., et al., *Quantum sensing and imaging with spin defects in hexagonal boron nitride.* Advances in Physics: X, 2023. **8**(1).
26. Zhou, J., et al., *Sensing spin wave excitations by spin defects in few-layer- thick hexagonal boron nitride.* Science advances, 2024. **10**(18): p. eadk8495-eadk8495.
27. Arcari, M., et al., *Near-Unity Coupling Efficiency of a Quantum Emitter to a Photonic Crystal Waveguide.* Physical review letters, 2014. **113**(9): p. 093603-093603.
28. Fröch, J.E., et al., *Photonic Nanostructures from Hexagonal Boron Nitride.* Advanced optical materials, 2019. **7**(4): p. n/a.
29. Li, C., et al., *Integration of hBN Quantum Emitters in Monolithically Fabricated Waveguides.* ACS photonics, 2021. **8**(10): p. 2966-2972.
30. Kim, S., et al., *Photonic crystal cavities from hexagonal boron nitride.* Nature communications, 2018. **9**(1): p. 2623-8.
31. Nonahal, M., et al., *Deterministic Fabrication of a Coupled Cavity–Emitter System in Hexagonal Boron Nitride.* Nano letters, 2023. **23**(14): p. 6645-6650.
32. Gangnaik, A.S., Y.M. Georgiev, and J.D. Holmes, *New Generation Electron Beam Resists: A Review.* Chemistry of materials, 2017. **29**(5): p. 1898-1917.
33. Fournier, C., et al., *Position-controlled quantum emitters with reproducible emission wavelength in hexagonal boron nitride.* Nature communications, 2021. **12**(1): p. 3779-3779.
34. Gale, A., et al., *Site-Specific Fabrication of Blue Quantum Emitters in Hexagonal Boron Nitride.* ACS photonics, 2022. **9**(6): p. 2170-2177.
35. Nonahal, M., et al., *Coupling spin defects in hexagonal boron nitride to titanium dioxide ring resonators.* Nanoscale, 2022. **14**(40): p. 14950-14955.
36. Wu, M., et al., *Nanocavity optomechanical torque magnetometry and radiofrequency susceptometry.* Nature Nanotechnology, 2017. **12**(2): p. 127-131.
37. Hausmann, B.J.M., et al., *Diamond nonlinear photonics.* Nature Photonics, 2014. **8**(5): p. 369-374.
38. Kim, J.-H., et al., *Hybrid Integration of Solid-State Quantum Emitters on a Silicon Photonic Chip.* Nano Letters, 2017. **17**(12): p. 7394-7400.
39. Bracher, D.O., X. Zhang, and E.L. Hu, *Selective Purcell enhancement of two closely linked zero-phonon transitions of a silicon carbide color center.* Proceedings of the National Academy of Sciences, 2017. **114**(16): p. 4060-4065.
40. Hinney, J., et al., *Efficient excitation and control of integrated photonic circuits with virtual critical coupling.* Nature communications, 2024. **15**(1): p. 2741-2741.
41. Knill, E., R. Laflamme, and G.J. Milburn, *A scheme for efficient quantum computation with linear optics.* Nature, 2001. **409**(6816): p. 46-52.
42. Shandilya, P.K., et al., *Hexagonal Boron Nitride Cavity Optomechanics.* Nano letters, 2019. **19**(2): p. 1343-1350.

43. Zheng, X.Q., J. Lee, and P.X.L. Feng, *Hexagonal boron nitride nanomechanical resonators with spatially visualized motion.* Microsystems & nanoengineering, 2017. **3**(1): p. 17038-17038.

For Table of Contents Only

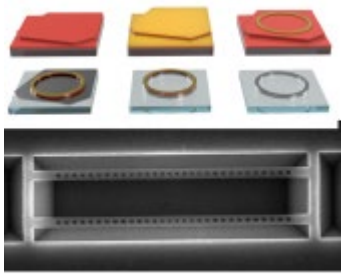

Supplementary Material:

Double Etch Method for the Fabrication of Nanophotonic Devices from Van der Waals Materials

Otto Cranwell Schaeper[1,2], Lesley Spencer[1,2], Dominic Scognamiglio[1], Waleed El-Sayed[3], Benjamin Whitefield[1,2], Jake Horder[1,2], Nathan Coste[1], Paul Barclay[3,4,5], Milos Toth[1,2], Anastasiia Zalogina[1,2*], and Igor Aharonovich[1,2*]

[1] *School of Mathematical and Physical Sciences, University of Technology Sydney, Ultimo, New South Wales 2007, Australia*

[2] *ARC Centre of Excellence for Transformative Meta-Optical Systems, University of Technology Sydney, Ultimo, New South Wales 2007, Australia*

[3] *Institute for Quantum Science and Technology, University of Calgary, Calgary, AB T2N 1N4, Canada*

[4] *Department of Physics and Astronomy, University of Calgary, Calgary, AB T2N 1N4, Canada*

[5] *Nanotechnology Research Centre, National Research Council of Canada, Edmonton, AB T6G 2M9, Canada*

[*]anastasiia.zalogina@uts.edu.au; igor.aharonovich@uts.edu.au

S1. Expended Double Etch Method

All the devices in this work were fabricated from pristine hBN flakes sourced from the National Institute for Materials Science (NIMS). HBN was mechanically exfoliated using Scotch tape and then transferred using a Gel-Pak onto 285 nm SiO_2 on Si. The samples were then annealed in a tube furnace (Lindberg Blue Mini-mite) in atmospheric conditions using the following recipe; initially, the temperature is rapidly ramped to 500°C where it remains at that temperature for 150 minutes, followed by a 10-minute ramp to 650°C where it remains for 75 minutes and finally, a 15-minute ramp to 850°C remaining at the temperature for for 40 minutes, then passively cooling to ambient temperature. The tube furnace anneal provides three essential benefits. Firstly, it increases the prevalence of UV emitters which are a prerequisite for B centers activation. Secondly, it increases the adhesion of the hBN flakes to the sample surface, and finally it removes residual resist contamination from the exfoliation.

A layer of 25 nm nickel was deposited into the substrate using an electron beam evaporator, (AJA ATC-1800E) (Figure S1 (c) i). Following this, a layer of PMMA A5 (AllResist gmbh) was spin-coated on the sample at 4000 rpm for 30 s, resulting in a layer of approximately 300 nm and then was baked at 180°C for 3 minutes (Figure S1 (c) ii). Due to the physical nature of the further ion beam etching step, the electron beam resist must be either sufficiently thick or resistive enough to withstand the etching. More resistive electron resists such as ma-N, Chemical Semi Amplified Resist (CSAR), or Hydrogen silsesquioxane (HSQ) could be used, although this has not been explored here. The pattern was defined with electron beam lithography (EBL) (Elionix ELS-F125), with an accelerating voltage of 125 keV and a beam current of 1nA. When using 1 nA of current, the spot size of 2.3nm and a step size of 2 nm were used to increase the resolution of the pattern. Following EBL the sample was developed in 1:3 IPA:MIBK for 60 s, rinsed in IPA for 20 s and gently dried with N_2. After development,

the sample is etched with ion beam etcher (IBE) (Intlvac) for 90 s using the following recipe: 6 sccm Ar, 1.5 A of discharge and 0.150 A of emission to the LFN, 12 sccm of Argon to the ion source, 400V beam voltage, 150 mA beam current, 60 V accelerator voltage, with a stage temperature of 20°C.

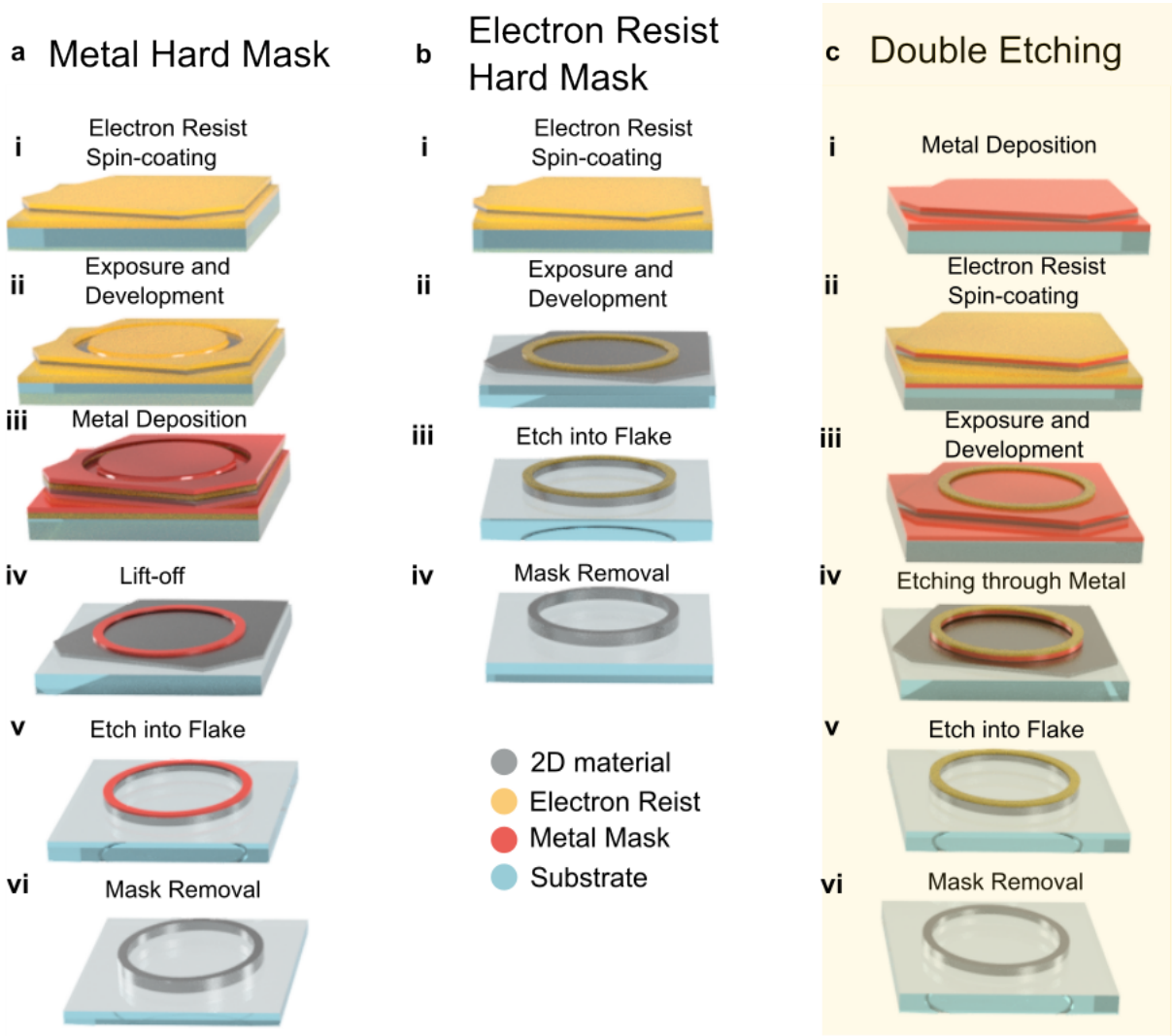

Figure S1. Comparison of different methods*. (a) Metal hard mask method, where (i) electron-resist is spin-coated onto the sample before (ii) being exposed and developed. (iii) Metal is then deposited onto the sample and (iv) lifted-off using a solvent stripper and sonication. (iv) The flake is etched using ICP RIE and then (vi) the metal mask is removed. (b) Electron-resist hard mask method, where (i) electron-resist is spin-coated onto the sample before (ii) being exposed and developed. (ii) The flake is etched using ICP RIE and then (iv) the mask is removed. (c) Double etch method where (i) metal is deposited onto the substrate before (ii) electron-resist is spin-coated. (iii) The resist is exposed and developed before (iv) using an IBE to etch through the exposed metal. (v) The revealed flake is etched using ICP RIE then (vi) the mask is removed.*

The patterned resist is used as a hard mask during this step, transferring the desired pattern into the nickel layer. Afterwards, the nickel and the residual resist are used as a hard mask for dry

etching. In this work, an an inductively coupled plasma reactive ion etcher (ICP-RIE) (Trion) was used to selectively etch the hBN with the following recipe: 1 mT, 1 W ICP, 300 W RF, 60 sccm Ar and 5 sccm SF_6, these conditions yield an etch rate of ~5 nm/s in hBN. Over the development of this method, the maximum etch time attempted was 7 minutes which did not exhaust the nickel layer, resulting in a minimum etch selectivity of 87:1 hBN to nickel. This high degree of selectivity is a major reason for the pursuit to develop this method, as when using a resist hard mask, the maximum dry etching depth using our conditions is ~400 nm. This increase in selectivity and, therefore, etch depth was critical for the development of devices that required an hBN thickness of 700nm. After the completion of dry etching, the nickel layer can readily be removed by submerging in various acid solutions; both 25% nitric acid and piranha solution (3:1 sulphuric acid to 30% hydrogen peroxide) were used. Other options such as nickel etchant or hydrofluoric acid could be used to remove the nickel whilst leaving the hBN unaffected. Once the nickel mask has been removed, V_B^- were generated in the microring region of Figure 2 (a) by an FEI DB235 Dual Beam FIB/SEM, using a 30 keV nitrogen ion beam to irradiate an area with a fluence of $1x10^{14}$ ions/cm^2.

S2. Comparison of Metal- and Resist-Hard Mask Methods

Firstly, we will briefly describe the basics of the two traditional methods in semiconductor fabrication depicted in Figure S1 (a) and (b), which have also been applied for the fabrication of vdW materials. The metal mask method (Figure S1(a)) starts with an electron resist spin-coating onto a vdW material (i) for EBL to expose the desired pattern (ii). Following the development of the resist, the metal mask is deposited (iii) to undergo the lift-off process (iv). The lift-off process removes the resist layer with the metal on top by submerging the sample into solution and a brief sonication afterwards to remove the residual metal. Afterwards, the pattern is transformed by etching through the vdW flake (v) and by removing the metal mask at the end (vi). The lift-off (iv) is the step where many works have reported the loss of vdW flakes due to insufficient vdW forces holding the flake to the substrate against the sonication.

Significant work with hBN has overcome this limitation by using the electron resist as the hard mask for the dry etching step. The advantage of this method is the elimination of the lift-off step. The primary limitation of this method is that the resist, even baked post development, is not as resistive as metal masks against the chemical or physical etching in an ICP RIE, bending feature designs if not being completely etched through. In addition to this, residual electron beam resist is challenging to remove after chemical and physical ion and plasma bombardment.

Figure S1 (b) depicts the workflow for the resist hard mask method. This method requires the least number of steps from start to finish and no deposition. The shortcomings that a resist hard mask receives in exchange for this simplicity are limited versatility and low etch selectivity. This is due to the similarity in composition of resists, rendering them unusable with oxygen chemistry and mildly resistant to fluorine chemistries. The low etch selectivity limits the use of electron beam resist hard mask to shallow etches with non-aggressive etch chemistries. Resulting in an electron beam resist hard mask only being viable in a few niche cases.

S3. Metal- and Resist- Hard Mask Methods Limitations

Metal-Hard Mask Method Limitation

Efforts were made to fabricate hBN devices using lift-off to define a metal hard mask. A layer of ~400 nm PMMA was spin-coated and a thin metal layer of 8 nm of titanium and 25 nm of nickel was deposited via electron beam evaporation. Reliable lift-off was not achieved due to two issues. The first issue was losing the entire flake when attempting to lift off the metal. The second issue was when the flake remained attached the metal lift-off was generally incomplete. Figure S2 (a-e) shows SEM images of failed lift-off steps, where both the large and the small features did not lift-off. Openings in the frame of the pattern were added to aid in the large feature lift-off, shown in Figure S2 (d), however the lift-off was not successful.

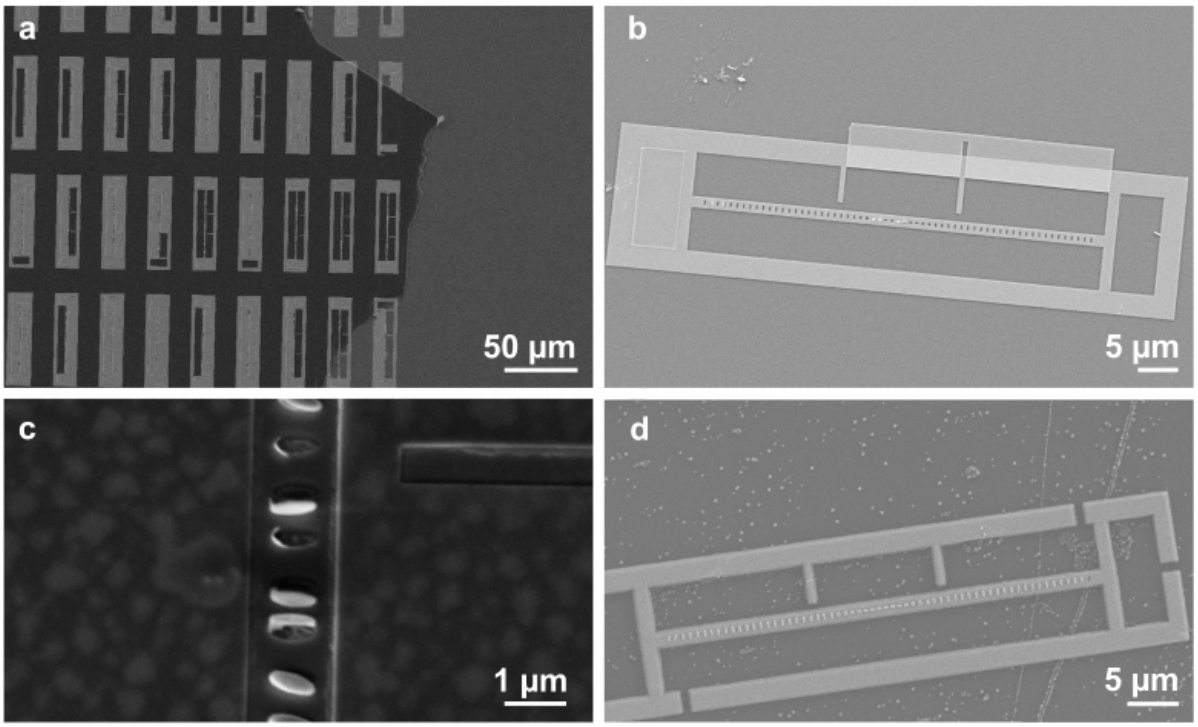

Figure S2. *SEM images showing lift-off on hBN flakes. (a) Demonstration of regions where the pattern was not revealed during the lift-off step. (b) Example of metal remaining fully and partially attached. (c) Demonstration of the small features on the device not lifting off. (d) an alteration to the pattern was made to aid in lift-off in the larger regions, this was successful but the small features remained unchanged.*

The removed metal mask would sometimes settle on top of the structures, and since any form of aggressive agitation is incompatible with vdW materials, it could not be removed (Figure S2 (d) and Figure S3). When the metal did fully lift-off, the resultant edges of the hard mask were quite rough. Figure S3 (a) shows an SEM image, where the device is tilted at 45°, with the metal hard mask still on the device. Surrounding the holes is excessive metal hard mask material which would affect the quality of the sidewalls and the geometry of the etched device.

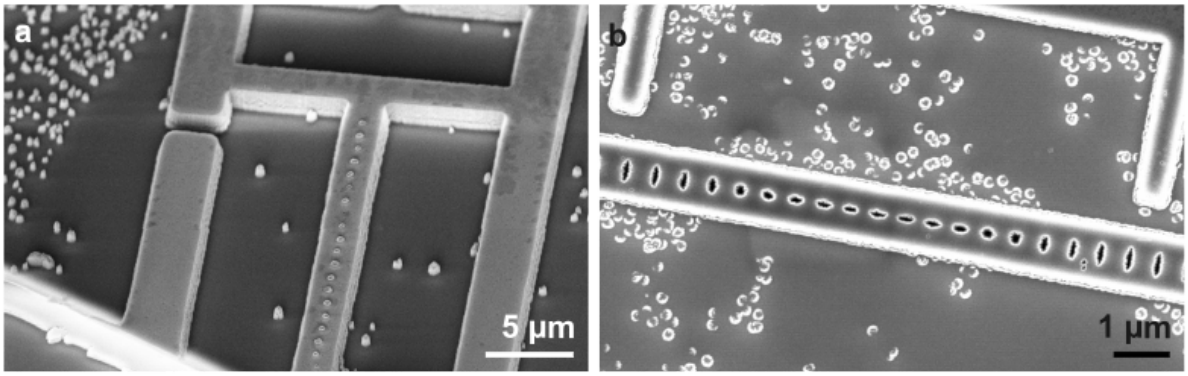

Figure S3. *SEM images demonstrating the most successful lift-off achieved with metal hard-mask method. (a) The raised regions of the metal mask were deposited on the resist sidewall. (b) Visibly rough side walls transferred into the hBN from the metal mask during ICP-RIE.*

Resist-Hard Mask Method Limitation

Fabrication of hBN devices using electron beam resist is widespread but usually features ICP-RIE recipes using CF_4 or CHF_3 as they are less abrasive. When using CSAR electron resist and SF_6 as the source for fluorine ions for ICP-RIE etching, we obtain a selectivity of ~6:5 hBN:CSAR. To increase the maximum possible etch depth a thicker layer of resist can be used. These solutions have a key drawback of requiring higher exposure dose for EBL, which increases the difficulty of patterning features that are either close together or small in size. Additionally, due to the scattering of electrons within the electron beam resist, the produced pattern in the resist can have sloped walls, which are transferred into the bulk material during etching. The main drawback of this method is resist-hard mask removal. The CSAR forms a compound with the fluorine ions when exposed to SF_6 plasma. This fluorinated resist is much more stable in the presence of resist solvents such as NMP or acetone. This effect is shown in Figure S4, where the regions of the resist most exposed to the plasma, the side walls, can resist being broken down in solvents.

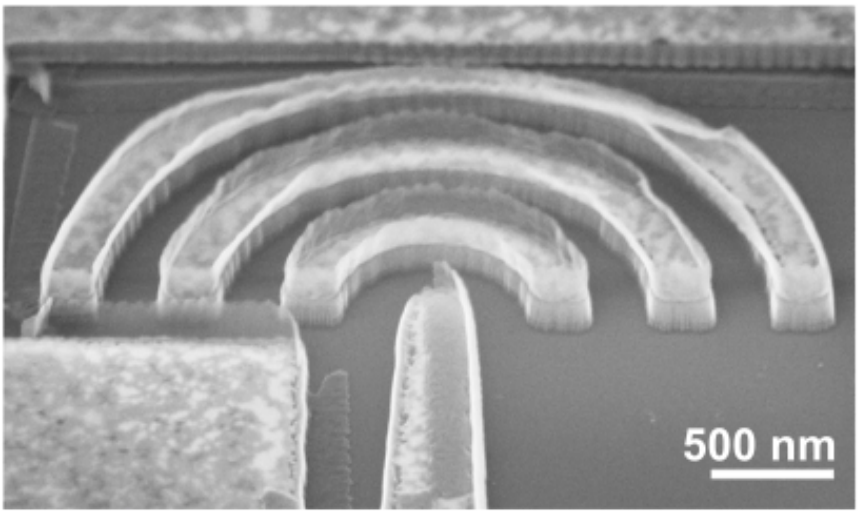

Figure S4. *Device where CSAR resist was used as the hard mask. This image is taken after ICP-RIE etching and attempting to remove the mask by soaking in 50°C NMP, and rinsing in acetone and IPA.*

S4. Characteristic of the Double Etch Method

When submerging in solutions or nitrogen blow drying, the unconnected surrounding flake would occasionally be displaced. This was easily avoided in the future by simply taking greater care when submerging or drying the substrate. However, the active device always remained in place, retaining the surrounding flake greatly aids in the distinguishability of the target area. The regions previously covered by the flake appear darker due to the remaining SiO_2, visible in Figure S5 (a).

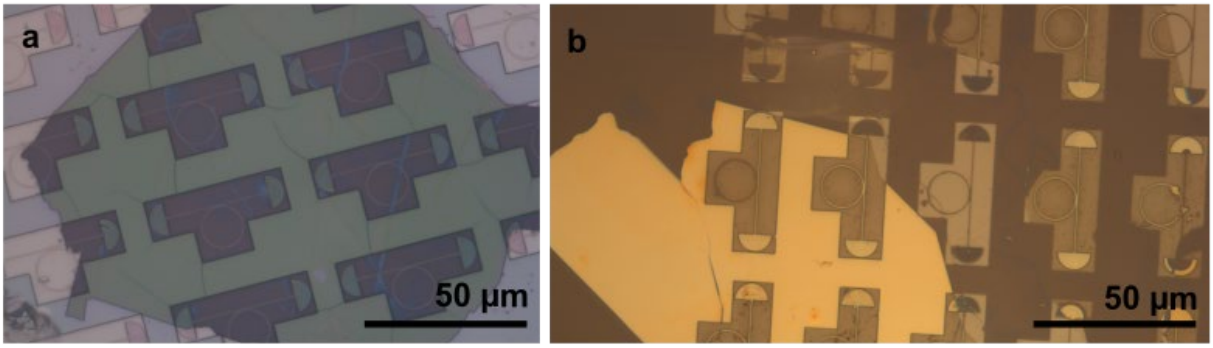

Figure S5. *Optical images of hBN flakes after mask removal. (a) Flake that completely remained in place. (b) Region where the flake became detached from the substrate.*

S5. SEM images of fabricated structures

Additional SEM images of the devices studied in the manuscript.

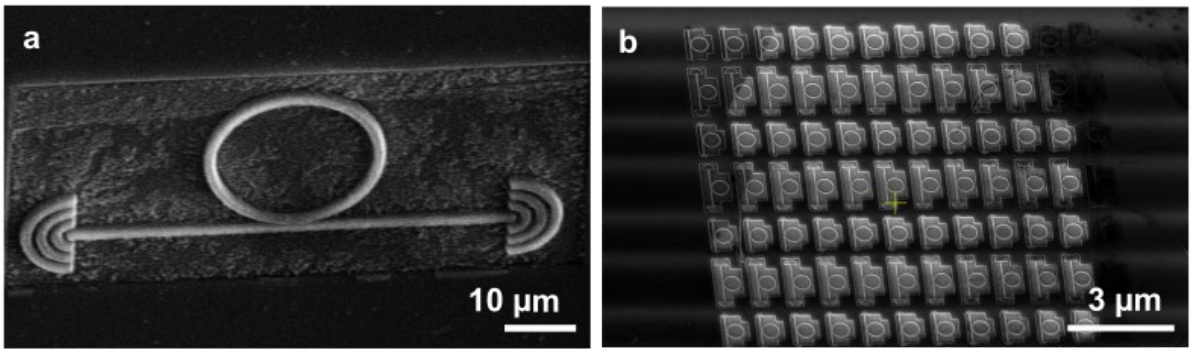

Figure S6. *SEM images of 45° tilted microring resonators. (a) Single structure. (b) Array of resonators.*

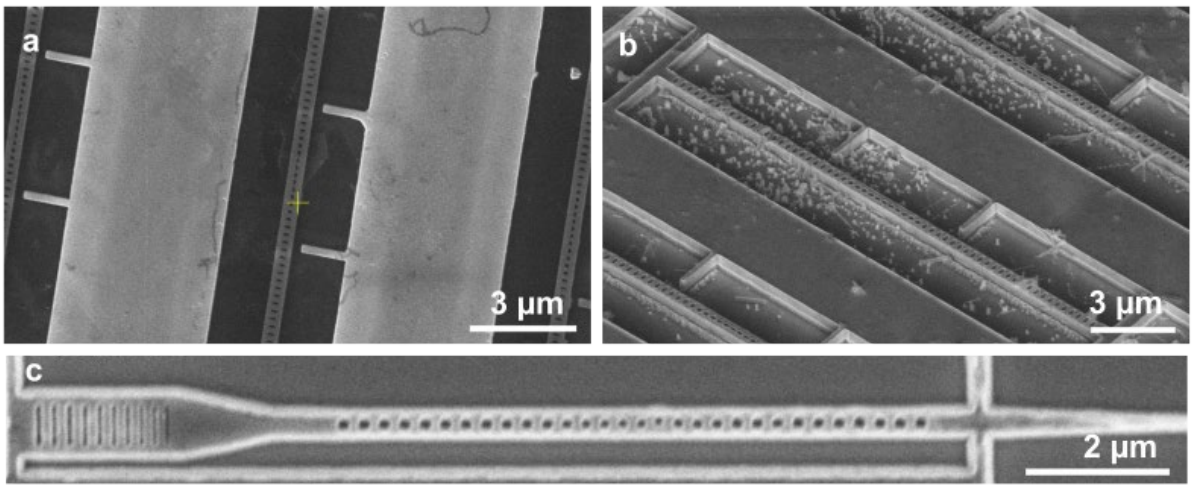

Figure S7. *SEM images of 1D PCC. Images of a device with the same geometry as the 1D PCC in Figure 2 (a) top-down & (b) sample tiled at 45° (c). (c) Top-down image of the device with the same geometry as shown in Figure 2. (d)*

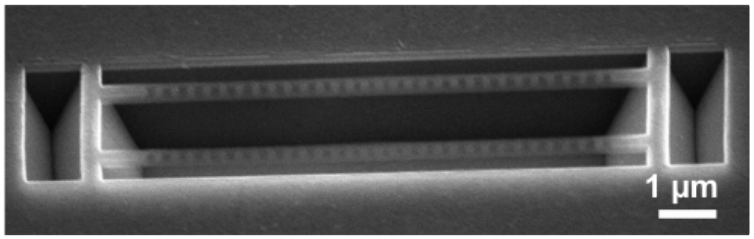

Figure S8. *An additional SEM image of the 1D PCC shown in Figure 2 (d), in this case the sample was tiled to 45° to better display the air gap.*

S6. Numerical Simulations of Optical and Mechanical Modes for 1D PCC

To demonstrate the versatility of our double etch method, we fabricated a larger structure at longer wavelengths as well. While smaller structures can be sensitive to fabrication imperfections, larger structures also present challenges, such as the etching of thicker vdW material flakes. To explore the telecom range, we designed a 1D photonic crystal cavity (PCC) structure. Although emitters in hBN have not yet been reported in this range, there is growing interest in exploring optomechanical systems in this range driven by mechanical resonances due to the ability of hBN to support the propagation of phonon polariton and light confinement at the deep subwavelength regime, which potentially enhance optical forces.

These systems are valuable for applications such as metrology, inertial and torque sensing, and the study of mechanical quantum fluctuations using conventional optical readout methods.

Our fabrication method serves as a versatile tool for different vdW materials, which may host emitters. To study optomechanical properties, we fabricated a 1D PCC for telecom applications due to the use of an infrared laser for detecting mechanical fluctuations. Achieving high sensitivity typically requires the co-localisation of optical telecom and mechanical modes with a high quality factor and maximized optomechanical coupling rate. The careful design of gap and hole parameters enables us to achieve this field localisation (Figure S9 below).

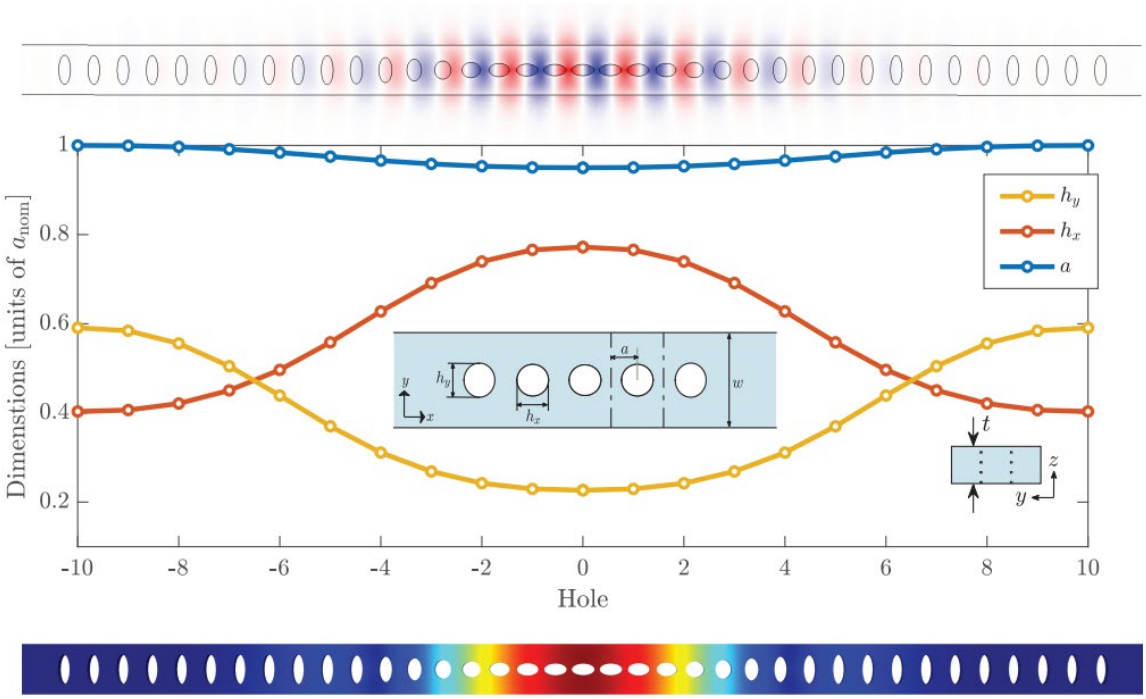

Figure S9. *Top: Electromagnetic field distribution of 1D PCC. Middle: Geometrical parameters for our structure, where h_y (yellow line) is the hole height, h_x (red line) is the hole width, and a (blue line) is the unit cell size. The width of 1D PCC (w) is 1000 nm, and the thickness (t) is 550 nm. Bottom: Electric field intensity spatial profile of the 1D PCC.*